

RESEARCH

Open Access



Taurochenodeoxycholic acid suppresses the progression of glioblastoma via HMGCS1/HMGCR/GPX4 signaling pathway in vitro and in vivo

Xiumin Xue^{1†}, Ziwan He^{1†}, Furui Liu¹, Qian Wang¹, Zhichao Chen¹, Lin Lin¹, Danni Chen¹, Yinfeng Yuan¹, Zihui Huang^{1*} and Yongjie Wang^{1*}

Abstract

Glioblastoma multiforme (GBM) is the foremost prevalent and highly aggressive intracranial malignancy, which urgently needs safer and more efficacious therapeutic strategies. Our research aimed to investigate the impact and the underlying mechanism of Taurochenodeoxycholic acid (TCDCA) on GBM. In this study, we explored the suppressive effect of TCDCA in vitro by qualification of proliferation and migration assays and flow cytometry, and subsequently predicted the potential anti-GBM mechanism of TCDCA by mRNA sequencing and the following rescue experiments. An orthotopic GBM model in C57BL/6 mice further demonstrated the anti-GBM mechanism of TCDCA. In vitro experiments verified that TCDCA inhibited the growth and migration of GBM cells and induced cell cycle arrest at the G2/M phase. Subsequent mechanism investigations showed that upregulation of HMGCS1 and HMGCR and downregulation of glutathione peroxidase-4 (GPX4) was observed in GBM cells by TCDCA treatment. Notably, inhibitory effects of proliferation and migration as well as induction of ferroptosis by TCDCA were partially restored by Simvastatin (SIN), a competitive HMGCR inhibitor. Furthermore, TCDCA showed an anti-GBM effect in an orthotopic transplantation model in vivo. TCDCA impedes GBM progression by virtue of this intricately orchestrated molecular cascade, through HMGCS1/HMGCR/GPX4 signaling axis, thus unveiling a novel therapeutic avenue warranting further scrutiny in the treatment landscape of GBM.

Keywords Taurochenodeoxycholic acid, Glioblastoma multiforme, Proliferation, Migration, Ferroptosis, HMGCR

Introduction

Glioblastoma multiforme (GBM) is the most common malignant primary brain tumor with an annual incidence of 3.21 per 100, 000 population in the United States [1,

2], and it is characterized by infinite cell proliferation, tissue invasion, tumor heterogeneity and angiogenesis [3, 4]. The current standard treatment for GBM is maximum surgical resection, accompanied by radiotherapy and chemotherapy with the classic drug temozolomide (TMZ) [5, 6]. Despite the maximal intervention, the prognosis of GBM remains poor, with a median survival of fewer than 15 months [7]. Furthermore, the treatment of GBM is a great challenge due to the existence of the blood–brain barrier (BBB) [8, 9]. Thus, there is an urgent need to explore new therapeutic drugs for GBM to improve the treatment outcomes of patients.

[†]Xiumin Xue and Ziwan He contributed equally to this work.

*Correspondence:

Zihui Huang
huang0069@hznu.edu.cn

Yongjie Wang
wangyongjie@hznu.edu.cn

¹ School of Pharmacy, Hangzhou Normal University, Hangzhou 311121, China



In recent decades, many cancer patients have used traditional Chinese medicine (TCM) as a replacement therapy for cancers because of its effectiveness and safety [10–13]. For example, in non-small-cell lung cancer therapy, the synergistic effect of Ginkgetin can improve the therapeutic effect of lung cancer patients by inducing ferroptosis of lung cancer cells [14]. The natural product baicalin exerts its anticancer activity by inducing FTH1-dependent ferroptosis [15]. Jatrorrhizine significantly inhibited the proliferation and metastasis of breast cancer cells [16]. Drug resistance is one of the greatest challenges in cancer treatment, and natural compounds of TCM have the potential to improve drug resistance in tumor cells.

Usually, treatment plans are developed for patients based on factors such as the condition, pathology type, stage, and physical condition. Currently, conventional treatment methods for cancer patients include surgical excision, chemotherapy [17, 18], radiotherapy, immunotherapy [19–23], and targeted therapy [24, 25]. A popular area of research is the control of carcinogenesis by altering the metabolism of cancer cells [26–29]. Numerous preclinical studies have demonstrated the anti-cancer effect of metabolic therapies by targeting cholesterol metabolism pathway in various tumors, such as GBM, breast cancer, prostate cancer, and colorectal cancer [30]. Large molecules like cholesterol cannot directly cross the BBB from the periphery to the central nervous system (CNS), the CNS maintains a relatively isolated microenvironment for cholesterol metabolism [31, 32]. Targeting cholesterol metabolism may be viewed as a potential adjuvant therapy for patients due to the distinct reprogramming pattern of cholesterol metabolism found in GBM.

HMG CoA reductase (HMGCR) is a protein of the endoplasmic reticulum (ER) membrane that catalyzes the conversion of HMG-CoA to mevalonate and is an important regulator of cholesterol metabolism [33, 34]. One of the prospective treatment approaches for cancer patients is to target HMGCR, which is involved in the progression of several malignancies, including breast, prostate, brain, and colorectal tumors [35]. A study has shown that the expression of HMG-CoA synthase 1 (HMGCS1, the upstream of HMGCR in cholesterol metabolism) and HMGCR which play a key role in cholesterol de novo synthesis, are reduced in GBM cells [36]. However, the expression pattern and the biological functions of HMGCR in GBM remained largely unknown.

As detergent molecules, bile acids are synthesized by the oxidation of cholesterol and are the major components of bile [37], which are increasingly being recognized as complex signaling factors rather than simply regulators of bile acid homeostasis [38]. Conjugation

with taurine or glycine can increase the solubility of bile acid [39], Taurochenodeoxycholic acid (TCDCA) is one of these forms. TCDCA is a potential anti-inflammatory drug and previous studies have demonstrated that TCDCA can be a potential therapeutic agent for rheumatoid arthritis (RA) or other inflammatory diseases by inhibiting the expression of pro-inflammatory cytokines such as interleukin-1 β (IL-1 β), IL-6, tumor necrosis factor- α (TNF- α) and inducing the apoptosis of fibroblast-like synoviocytes (FLS) [40]. It has been reported that TCDCA has immunomodulatory activity, which can significantly enhance the phagocytic function of the monocyte-macrophage system and inhibit hypersensitivity [41]. TCDCA not only demonstrates great therapeutic potential in anti-inflammatory and immune regulation but also contributes to the therapy of tumors by greatly inhibiting the growth and invasion of gastric cancer cells and triggering their apoptosis [42]. Given the unique structure of TCDCA, it is a conjugated bile acid with higher water solubility than UDCA [43], which is primarily used in hepatobiliary diseases. Moreover, previous studies have shown that TCDCA improves the progression of Experimental Autoimmune Encephalomyelitis by regulating the TGR5-mediated AKT/NF- κ B signal pathway to inhibit neuroinflammation of astrocytes [44]. These studies suggest that TCDCA has the potential to cross the BBB and play a role in treating related diseases. However, its roles in GBM cells remain unclear.

In this study, we aimed to investigate the anti-GBM potential effects of TCDCA and elucidate the underlying molecular mechanisms. Our results showed that TCDCA effectively inhibited the proliferation of GBM cells by cell cycle arrest at the G2/M phase and migration of GBM cells. Furthermore, we found that TCDCA's anti-GBM effects were mediated through the activation of the HMGCS1/HMGCR/GPX4 signaling pathway both *in vitro* and *in vivo*.

Materials and methods

Cell culture

The C6 glioma cell line was kindly provided by Professor Maojin Yao from Sun Yat—Sen University, the HT22 cell line was generously provided by doctor Xian Zheng from China Pharmaceutical University, and the U251 cell line was purchased from Procell Life Science & Technology Co., Ltd. Prior to use, all cell lines were authenticated via short-tandem repeat (STR) profiling and tested for mycoplasma contamination to ensure its authenticity and integrity. The cells were cultured in Dulbecco's modified Eagle's medium (DMEM), supplemented with 10% FBS (SERANA, Mexico), 1% penicillin/streptomycin (Gibco, Grand Island, America) and aseptically grown in a humidified incubator containing 5% CO₂ at 37 °C.

Animals

The animal study was reviewed and approved by the Animal Ethics and Welfare Committee at Hangzhou Normal University (Approval No.: HSD20220105). Female C57BL/6 mice (18–22 g, 6–8 weeks old) were purchased from Shanghai SLAC Laboratory Animal Co., Ltd. (Shanghai, China) and transported to the Laboratory Animal Center of Hangzhou Normal University after passing the quality inspection. Mice were housed under standard laboratory conditions (temperature 22 ± 2 °C, humidity 50–60%) and provided with food and water ad libitum.

Drugs

Taurochenodeoxycholic acid sodium salt (TCDCa) was purchased from MCE (HY-N1429, Shanghai, China). Stock solutions of 100 mM were prepared in Dimethyl sulfoxide (DMSO) and stored at -80 °C until use. The final concentration of DMSO is 0.2%. Both Simvastatin (HY-17502, Shanghai, China) and Ferrostatin-1 (HY-100579, Shanghai, China) were purchased from MCE and diluted with DMSO into 1 mM stock solution. For in vivo administration, TCDCa stock solutions were prepared at a concentration of 300 mg/mL in sterile saline and stored at -80 °C until use. For each injection, a working solution was freshly prepared by diluting the stock solution to a concentration of 30 mg/kg in saline.

GlioVis analysis

This database (<http://gliovis.bioinfo.cnio.es/>) can be used for a variety of other analyses in addition to gene expression studies: survival, association, mutation, etc. We used this website to analyze the differential expression of genes of interest in normal and glioma patient tissues. The Chinese Glioma Genome Atlas (CGGA) (<http://www.cgga.org.cn/>) is a comprehensive online resource for the molecular characterization and analysis of gliomas, to browse *HMGCS1* and *HMGCR* mRNA expression profiles and to perform survival analysis in different grade gliomas.

RNA-Seq

Three paired groups of U251 cells treated with or without TCDCa were sent to Novogene (Beijing, China) for RNA-sequencing. The raw data is accessible through accession number GSE236200 (<https://www.ncbi.nlm.nih.gov/geo/>).

Cell viability assay

Cell viability was assessed by using the Cell Counting Kit-8 (CCK-8, FD3788, Fdbio science; Hangzhou, China). GBM cell lines were seeded into 96-well, flat-bottomed plates at 3000 cells/well and incubated overnight. After 24 h starvation with medium containing 1% serum, the mother liquor of TCDCa (100 mM) was diluted to 100, 200 and 400 μ M in the medium containing 1% FBS for 24 h. Additionally, the viability of U251 cells treated with 200 μ M TCDCa was assessed in combination with Simvastatin (SIN) at concentrations of 0.5 μ M, 1 μ M, and 5 μ M, and Ferrostatin-1 (FER-1) at concentrations of 0.5 μ M, 1 μ M, 1.25 μ M, 1.5 μ M, 2 μ M, and 2.5 μ M. Finally, cells were incubated for an additional 2 h in the medium with 10% CCK-8. The absorbance at 450 nm was measured in a microplate reader (Multiskan FC, Thermo Scientific, USA).

Colony formation assay

The C6 cells and U251 cells at 1000 cells/well were seeded onto 6-well plates and cultured in 10% serum medium with 200 μ M TCDCa. The medium was changed every two days until obvious colonies were formed. In the end, the supernatants were removed and the cells were washed with phosphate buffered saline (PBS) twice with 5 min/time. Cells were fixed and treated in 4% paraformaldehyde solution for 20 min and stained with 1% crystal violet. After removing the staining solution, the colonies were washed with PBS, inverted on absorbent paper and dried. Then air-dried or dried at 37°C, 0.5 ml of 33% acetic acid was added to each well, and the decolorization absorbance was measured at 570 nm using a microplate reader (Varioskan Flash, Thermo Scientific, USA) after vibration.

Cell cycle by flow cytometry

The C6 cells and U251 cells were cultured in 6-well plates with 1×10^6 cells per well and treated as per experiment requirements when cell growth reached 60–70% and continued to culture in 1% serum medium for 24 h with 200 μ M TCDCa. After the treatment, cells were washed twice with cold PBS, then transferred to a 1.5 mL centrifuge tube and centrifuged at $200 \times g$ for 5 min. After discarding the supernatant, cells were dehydrated with 75% ethanol overnight at 4 °C, centrifugation was conducted at $200 \times g$ for 5 min to collect the cells. After added about 1 mL of precooled PBS, the cells were resuspended, centrifuged, and reprecipitated again to remove residual ethanol. Following the manufacturer's instructions (Cell Cycle Staining Kit, Multi Sciences, CCS012), the pelleted cells were re-suspended in DNA staining solution,

incubated in the dark for 30 min, and then tested cell cycle by using a flow cytometer (CytoFLEX S, Beckman Coulter, USA). The results were processed with FlowJo software and the number of cells in each phase was expressed as a percentage.

Western blot

Cold RIPA buffer (P0013B; Beyotime) containing protease inhibitors was used to extract the whole protein. The extracted protein was quantified with BCA working solution and combined with 5× loading buffer, and boiled the obtained protein sample at 100 °C for 20 min with a metal bath. Cell lysate (30 µg) was loaded on sodium dodecyl sulfate–polyacrylamide gel electrophoresis (SDS-PAGE) and transferred onto PVDF membranes. Membranes were blocked with 5% skim milk in TBST for 1 h at RT, and rinsed three times for 15 min with TBST. The immunoblots were incubated with different primary antibodies at 4 °C for 12 h, probed with secondary antibody, and rinsed again three times for 15 min in TBST. The proteins were visualized using an ECL detection kit (#FD8020, FDBio, Hangzhou, China). For statistical analysis of the relative expression of target proteins, the bands were processed using ImageJ software. The gray values of the corresponding exposure bands were calculated by the software. The relative expression of each protein was then determined by normalizing the gray values of the target proteins to those of the internal reference proteins (e.g., GAPDH or β-actin) for each sample. Primary antibodies included rabbit anti-HMGCR (ET1702-41, huabio, 1:1000), rabbit anti-HMGCS1 (ab155787, Abcam, 1:1000), rabbit anti-GPX4 (52455 s, CST, 1:1000), mouse anti-GAPDH (200,306-7E4, Zenbio, 1:5000), mouse anti-Vimentin (ab8978, Abcam, 1:1000), rabbit anti-N-cadherin (ER0503, huabio, 1:1000), rabbit anti-FAK (3285T, CST, 1:1000), rabbit anti-p-FAK (T55587, Abmart, 1:1000) and mouse anti-β-tubulin (ET1602-4, huabio, 1:5000).

Reactive oxygen species (ROS) assay

In 12-well plates, 2×10^5 cells in the logarithmic growth phase were planted per well. After 24 h starvation with medium containing 1% serum, cells were then cultured in 1% serum medium for 24 h with 200 µM TCDCA. U251 cells were harvested with trypsin and incubated with 5 µM DCFH-DA at 37 °C for 30 min. DCFH-DA was nonfluorescent and produced a fluorescent signal after oxidation to DCFH in the presence of intracellular ROS (C390, Apexbio, Beijing, China). Fluorescence intensity was detected by flow cytometry and the results were analyzed by FlowJo software.

GSH and GSSG assay

U251 cells in logarithmic growth phase were seeded at 3×10^5 cells per well in 12-well plates. After 24 h starvation with medium containing 1% serum, cells were then cultured in 1% serum medium for 24 h with 200 µM TCDCA. The levels of glutathione (GSH) and oxidized glutathione disulfide (GSSG) in the cells were detected by kits according to the manufacturers' instructions (S0053 and S0052, Beyotime, Shanghai, China).

Transwell and wound-healing assays

For the Transwell migration assay, C6 cells and U251 cells in the logarithmic growth phase were digested with trypsin and the cell suspension concentration was adjusted to 1×10^5 /mL with serum-free medium. 200 µL cell suspension was placed in the upper chamber of Transwell (Corning), then cells were cultured with 200 µM TCDCA for 24 h. Finally, cells were fixed and stained with 1% crystal violet after 30 min of culture and photographed using a Nikon light microscope (Model Eclipse Ci-S; Nikon Corporation, Japan). For the wound-healing assay, cells were cultured in 12-well plates, 95% confluent monolayers were scratched with a sterile 200 µL pipette tip, and then cultured in a DMEM medium containing 1% serum. And the scratch heal rate after 24 h of culture was recorded.

Immunofluorescent staining

C6 cells and U251 cells slides were placed on the bottom of 12-well empty plates and cells were seeded at a density of 3×10^4 per well, and treated with 200 µM TCDCA or solvent for 24 h. The cells were washed twice with PBS, fixed in 4% PFA for 20–30 min. Then they were treated with 5% bovine serum albumin (BSA) and 0.1% Triton X-100 in PBS for 1 h at RT. Subsequently, the cells were incubated with primary antibodies (mouse anti-PH3, ab14955, Abcam, 1:2, 500) at 4 °C overnight. After being washed, cells were incubated with secondary antibody Fluorescein-conjugated goat anti-rabbit IgG for 1 h at RT. After washed with PBS three times for 5 min each, the anti-fluorescence decay mounting medium (S2100, Solarbio, Beijing, China) was dropped on the slide and mounted. Cells were observed under an Olympus VS200 microscopy and ImageJ software was used for analysis.

The tumoral tissues were collected and fixed in 4% PFA. Frozen sections were prepared and tissues were cut into 20 µm slices. The slices were rinsed in 1×PBS buffer three times, for 5 min each. They were then fixed again in 4% PFA for 20–30 min. Subsequently, the slices were placed in a blocking solution containing 5% BSA and 0.3% Triton X-100 in PBS for 1 h at RT. The tissues were incubated with the primary antibody (Rabbit anti-Ki67, A23722, ABclonal, Wuhan, China) at 4 °C overnight.

Afterward, the tissues were washed with 1×PBS. They were then incubated with the corresponding secondary antibody, Fluorescein-conjugated goat anti-rabbit IgG, for 1 h at RT. The tissues were washed again with PBS three times, for 5 min each. An anti-fluorescence decay mounting medium (S2100, Solarbio, Beijing, China) was applied to the slides and mounted. Finally, the tissues were sealed with neutral resin and observed under a confocal scanning imaging system (Nikon AX R MP with NSPARC, Nikon, Japan).

Quantitative real-time PCR (qPCR)

RNA was isolated with the RNA-easy Isolation Reagent (R701, Vazyme, Jiangsu, China), and cDNA was synthesized using the HiScript® II Q RT SuperMix (R223-01, Vazyme, Jiangsu, China) for reverse transcription PCR according to the manufacturers' instructions. SYBR Green PCR master mix (Q511-02/03, Vazyme, Jiangsu, China) was used for qPCR. Using specified primers, the Real-Time PCR Detection System (CFX Connect™ Optics Module, Bio-Rad, Singapore) was used to test the PCR amplification of the target and internal control (GAPDH) cDNA. Real-time PCR cycling conditions were programmed as follows: first step (95 °C, 15 min), cycling step (denaturation 94 °C, 15 s, annealing at 56 °C or 60 °C for 30 s, and final extension at 72 °C for 30 s×38 cycles). The individual PCR products were identified using melting curves at the end of the PCR programme.

The primers used in this study were synthesized by the Tsingke Biotech as follows (F: forward primer; R: reverse primer):

ATF3 (F): 5'-CCTCTGCGCTGGAATCAGTC-3';
 (R): 5'-TTCTTTCTCGTCGCCTCTTTT-3';
HMGCS1 (F): 5'-GATGTGGGAATTGTTGCCCTT-3';
 (R): 5'-ATTGTCCTGTTCCTCAACTTCCAG-3';
 β -actin (F): 5'-CATGTACGTTGCTATCCAGGC-3';
 (R): 5'-CTCCTTAATGTCACGCACGAT-3';
ASNS (F): 5'-GGAAGACAGCCCCGATTTACT-3';

(R): 5'-AGCACGAACTGTTGTAATGTCA-3';
GADD45A (F): 5'-GAGAGCAGAAGACCGAAA
 GGA-3';
 (R): 5'-CACAAACACCACGTTATCGGG-3';
LDL (F): 5'-TCTGCAACATGGCTAGAGACT-3';
 (R): 5'-TCCAAGCATTTCGTTGGTCCC-3';
HMGCR (F): 5'-TGATTGACCTTTCAGAG
 CAAG-3';
 (R): 5'-CTAAAATTGCCATTCCACGAGC-3';
MVD (F): 5'-CTCCCTGAGCGTCACTCTG-3';
 (R): 5'-GGTCCTCGGTGAAGTCCTTG-3';
ID11 (F): 5'-AACACTAACACCTCGACAAGC-3';
 (R): 5'-AGACACTAAAAGCTCGATGCAA-3';
CHAC1 (F): 5'-GAACCCTGGTTACCTGGGC-3';
 (R): 5'-CGCAGCAAGTATTC AAGGTTGT-3'.

Orthotopic transplantation mouse model

10 μ L GL261-luciferase cells (1×10^5 cells per mouse) were injected into the striatum (X=-1.8 mm, Y=0.6 mm, Z=3.8 mm) of the mice at a rate of 0.1 μ L/min using a digital stereotaxic device (RWD, Shenzhen, China). To prevent cell leakage, the needle was paused for 5 min after injection, and then it was lifted up by 0.02 mm and stopped for 5 min again. After one week of transplantation, the mice were randomly divided into two groups: the control group and the TCDCA group. Saline and 30 mg/kg TCDCA were administered daily for 14 d, by intraperitoneal injection per day. On 14th day of administration, the fluorescence intensity of the tumor was analyzed using an in vivo fluorescence imaging scanner in mice (PhotonIMAGER Optima, Biospace Lab, France). All mice were sacrificed 21 d after transplantation, the brains were collected for HE staining and western blot detection.

Hematoxylin-eosin (H&E) staining

The tumors, hearts, livers, lungs, spleens and kidneys were collected and fixed in 4% PFA. The frozen sections were then made and the tissues were subsequently cut

(See figure on next page.)

Fig. 1 TCDCA inhibited the proliferation and migration of GBM cells. **A** Molecular structural formula of TCDCA. **B, C** The cell viability of C6 cells (**B**) and U251 cells (**C**) treated with different concentrations of TCDCA detected by CCK-8 assays ($n=5$ /group, one-way ANOVA, Tukey's test was performed for the multiple comparison). **D** Representative images of C6 cells treated with 200 μ M TCDCA for 1 week in the colony formation assays. Scale bars, 5 mm. **E** Quantitative analysis of colony number (the surviving colonies > 50 cells) as shown in (**D**) ($n=3$ /group, t -test). **F** Representative images of U251 cells treated with 200 μ M TCDCA for 1 week in the colony formation assays. Scale bars, 5 mm. **G** Quantitative analysis of colony number (the surviving colonies > 10 cells) as shown in (**F**) ($n=3$ /group, t -test). **H, J** Representative images of PH3 staining (red) in C6 cells and U251 cells after treated with vehicle control or 200 μ M TCDCA for 48 h. Scale bars, 50 μ m. **I, K** Quantitative analysis of the percentages of PH3⁺ cells over total C6 cells and U251 cells in one field as shown in (**H, J**) ($n=15$ /group, t -test). **L, N** Representative images of C6 cells and U251 cells treated with 200 μ M TCDCA in wound healing assays. Phase-contrast images were acquired at 0 h, 24 h after scratching and representative images of three independent experiments were shown. Scale bars, 200 μ m. **M, O** Quantitative analysis of the wound healing area of C6 cells and U251 cells treated with TCDCA as shown in (**L, N**) ($n=12$ /group, t -test). **P, R** Representative images of C6 cells and U251 cells treated with 200 μ M TCDCA for 24 h in Transwell migration assay. Scale bar, 100 μ m. **Q, S** Quantitative analysis of the numbers of migrated C6 cells ($n=15$ /group, t -test) and U251 cells ($n=15$ /group, t -test) counted in representative high-power fields per Transwell plate. Data were mean \pm SEM. * $P < 0.05$, ** $P < 0.01$

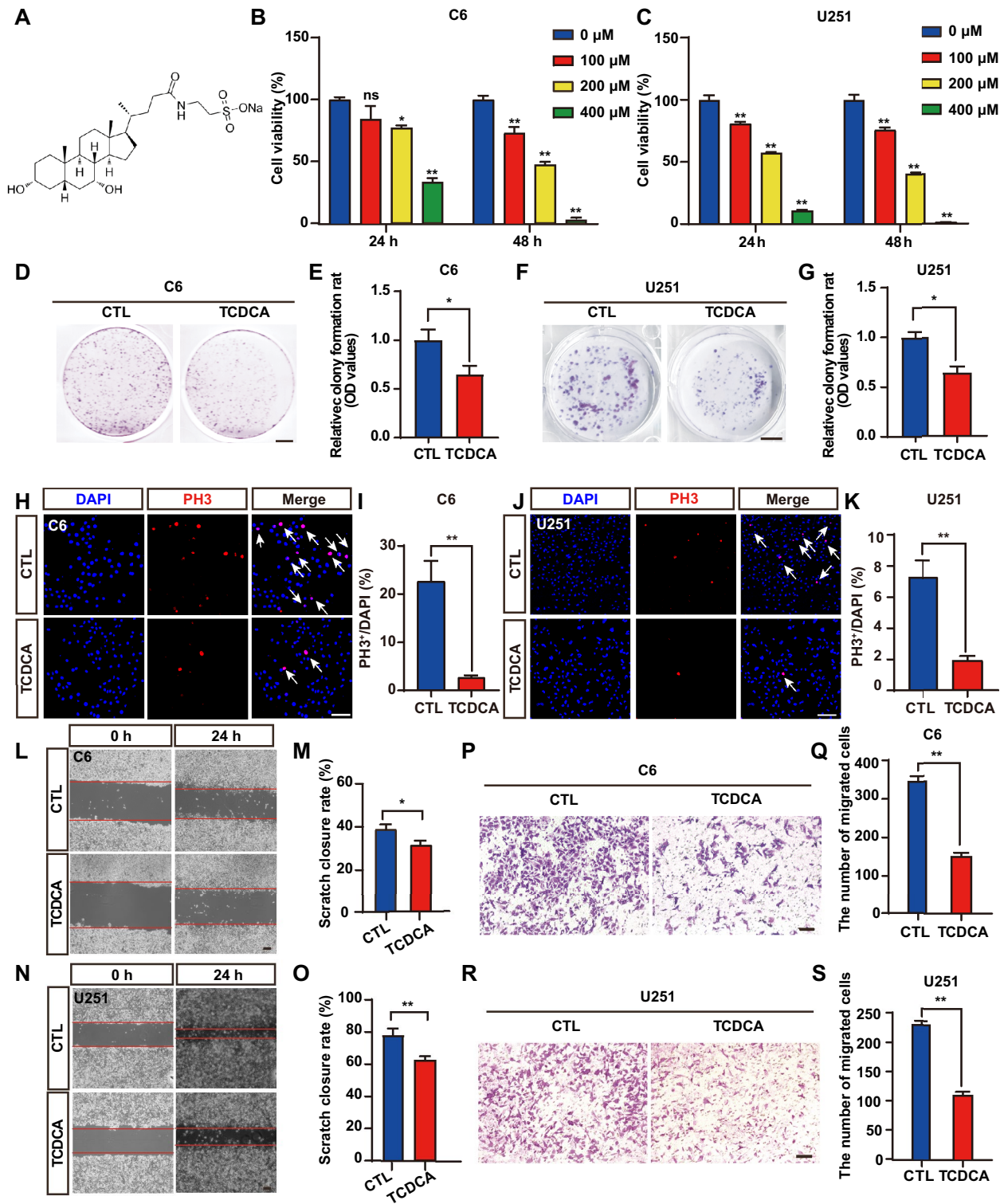


Fig. 1 (See legend on previous page.)

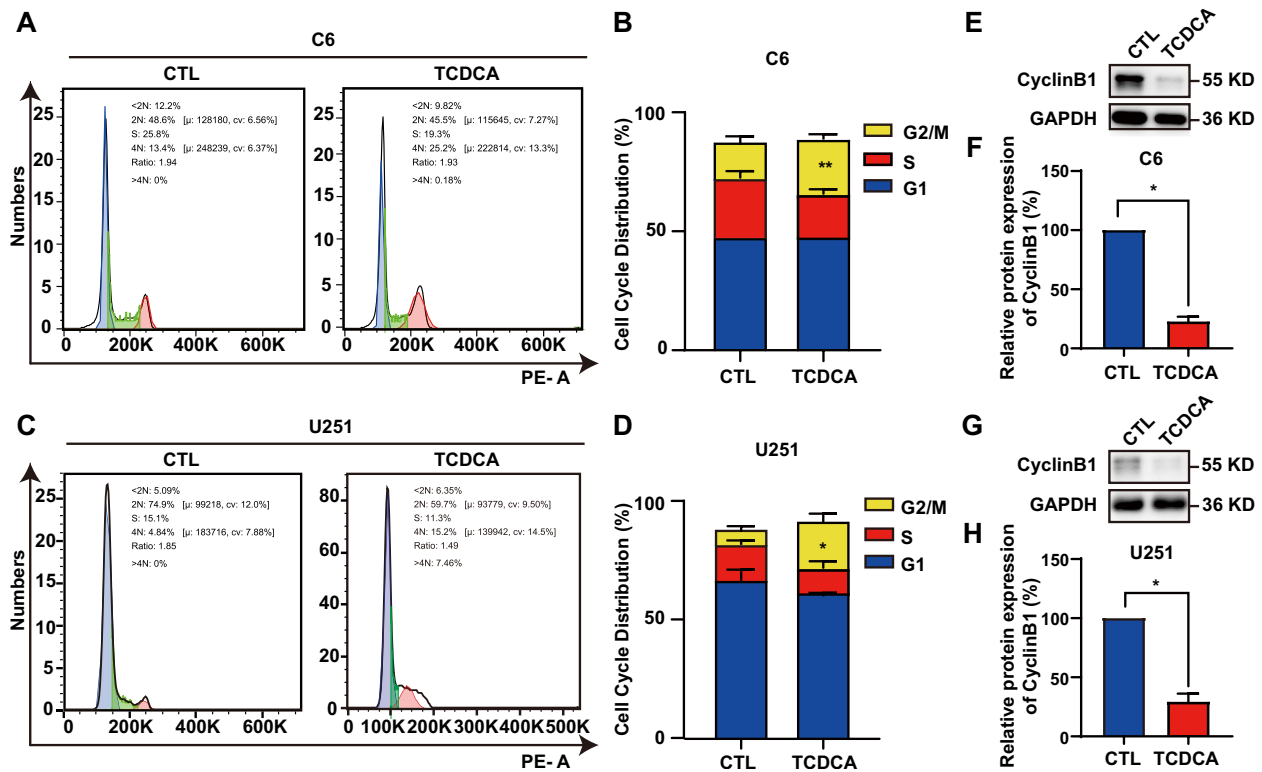


Fig. 2 TCDCA arrested cell cycle of GBM cells at G2/M phase. **A** Representative flow cytometry results of cell cycle (**A**) and quantitative analysis in C6 cells after 200 μ M TCDCA treatment for 24 h (**B**, $n = 3/\text{group}$, t -test). **C**, **D** Representative flow cytometry results of cell cycle (**C**) and quantitative analysis in U251 cells after TCDCA treatment for 24 h (**D**, $n = 3/\text{group}$, t -test). **E** The expression of Cyclin B1 in C6 cells was detected after treated with 200 μ M TCDCA for 24 h by western blot. **F** Quantification analysis of the relative Cyclin B1 level as shown in (**E**) (normalized to control, $n = 4/\text{group}$, Mann–Whitney test). **G** The expression of Cyclin B1 in U251 cells was detected after treated with 200 μ M TCDCA for 24 h by western blot. **H** Quantification analysis of relative Cyclin B1 level as shown in (**G**) (normalize to control, $n = 4/\text{group}$, Mann–Whitney test). Data were mean + SEM. * $P < 0.05$, ** $P < 0.01$

into 20 μ m slices. These sections were first stained in hematoxylin solution and soaked in sterile distilled water for 20 min, followed by staining in eosin solution. Then 75% ethanol, 95% ethanol, and 100% ethanol were used to dehydrate the sections, then the sections were treated in xylene for 10 min. Finally, tissues were sealed with neutral resin and observed under an Olympus VS200 microscopy.

Statistical analysis

All data are presented as the mean + standard error of mean (SEM) from at least three independent experiments. Statistical comparisons were made using t -test, Mann–Whitney test, one-way ANOVA, two-way ANOVA or two-way RM ANOVA. Tukey or Sidak's test was used for post hoc comparison. In all cases, $P < 0.05$ was considered statistically significant. All statistical analysis was conducted with GraphPad Prism 8 software.

Results

TCDCA inhibited the proliferation and migration of GBM cells in vitro

One of the characteristics of malignant glioma cells is uncontrolled division and proliferation. Firstly, we investigated whether TCDCA could inhibit the proliferation of C6 and U251 cells (two GBM cell lines) in vitro by cell counting kit-8 (CCK-8) assays. The result showed that TCDCA significantly reduced cell viability of GBM cells in time- and dose-dependent manners. To determine the IC₅₀ values of TCDCA in C6 and U251 cells, we treated the cells with various concentrations (0, 100, 200, 400 μ M) of TCDCA. We then measured cell survival using the CCK8 assay. The concentration–response data were analyzed using GraphPad Prism software. Specifically, we performed a logarithmic transformation of the drug concentrations and used the "nonlinear regression" function to fit the data to a dose–response curve. The software automatically calculated the IC₅₀ values based on this curve. Further analysis of the drug sensitivity curve results demonstrated that the half-inhibitory

concentration (IC₅₀) of TCDCA for C6 and U251 cells were 217.53 μ M and 205 μ M, respectively. Therefore, a concentration of 200 μ M was selected for subsequent experiments with the final concentration of DMSO used to treat the cells was 0.2% (Fig. 1B, C). We chose this concentration for subsequent experiments to ensure that we were working within a biologically relevant range while avoiding excessive cytotoxicity. Additionally, the 24-h time point was selected for evaluation because it provided a significant and measurable difference in cell viability, allowing us to observe the effects of TCDCA clearly. This concentration and time point were selected to balance the need for a robust experimental signal with the practical considerations of experimental design.

To ensure that the DMSO did not introduce any confounding effects on cell viability, we conducted a separate cell viability assay using the CCK8 assay on GBM cells, and found that 0.2% DMSO had no significant toxicity to GBM cells, confirming that the observed effects in our experiments were due to the tested compounds rather than DMSO itself. (Supplementary Fig. 1A). Meanwhile, we have conducted a toxicity test of TCDCA on HT22 cells, which are non-cancerous murine hippocampal neuronal cell line. The results demonstrate that TCDCA does not exhibit significant toxicity to HT22 cells at the concentrations used in our study (Supplementary Fig. 1B). This finding suggests that TCDCA selectively targets cancerous glioblastoma cells without adversely affecting normal neuronal cells. Tumor cells have a strong ability to adapt to the cultural environment and survive independently with strongly proliferative ability of cells characterized by increased number of colonies. As expected, when treated with 200 μ M TCDCA, the numbers of colonies formed by U251 and C6 cells were significantly decreased, compared with that of the control-treated cells (Fig. 1D–G). To further confirm the inhibitory effect of TCDCA on the proliferation ability of U251 and C6 cells, immunofluorescence staining showed that the percentage of PH3⁺ (a marker that labels cells in mitosis) cells was significantly decreased after being treated with TCDCA (Fig. 1H–K). Consequently, these results

suggested that TCDCA effectively suppressed the proliferation of GBM cells in vitro. Glioblastoma cells not only proliferate in the primary tissue but also migrate into other tissues and organs through blood vessels or lymphatic vessels, with strong migration ability [45–47]. To further investigate whether TCDCA could inhibit the migration ability of GBM cells in vitro, the wound-healing and Transwell experiments were performed. Wound-healing assay results showed that the wound closure of C6 and U251 cells was significantly reduced after treatment with 200 μ M TCDCA for 24 h, compared with that in controls (Fig. 1L–O). We then performed a Transwell assay, which can mimic the process of cell migration in vivo to a certain extent. Consistent with that in the wound-healing assay, the results showed that both C6 and U251 cells migrated through the filter after being cultured for 24 h in control group while the number of migrating cells in TCDCA treated cells was significantly reduced (Fig. 1P–S). These results suggested that TCDCA suppressed the migration of GBM cells in vitro.

TCDCA induced cell cycle arrest at the G₂/M phase of GBM cells.

The mitotic cell cycle is divided into interphase and M phase [48]. All cancers rely on continuous cell division, and increasingly rely on cell cycle control mechanisms to prevent infinite cell division [49]. To further explore whether the inhibition of proliferation in GBM cells is related to cell cycle arrest, flow cytometric assay was performed. Both C6 and U251 cells treated with TCDCA were arrested at the G₂/M phase of the cell cycle, and the percentage of cells in G₂/M was increased by TCDCA treatment (Fig. 2A–D). Cyclin B1 protein's synthesis, degradation and subcellular localization play an important role in mitotic regulation, and its decreased expression will lead to cell cycle arrest in G₂/M phase [50]. To further investigate this mechanism, western blot analysis was used to examine changes in Cyclin B1 expression following the action of TCDCA. As expected, the expression of Cyclin B1 was indeed significantly decreased in C6 and U251 cells after the treatment with TCDCA (Fig. 2E–H).

(See figure on next page.)

Fig. 3 TCDCA upregulated lipid biosynthetic process in GBM cells. **A, B** GO and reactome dot enrichment analysis of genes significantly altered in U251 cells after treatment with 200 μ M TCDCA for 24 h. **C** Representative heat map of the upregulated and downregulated genes in 200 μ M TCDCA-treated U251 cells compared with that in the control-treated cells. The depth of red represents the level of gene expression. The expression of several genes such as *HMGCS1* and *HMGCR* were increased significantly. **D** The volcano plot showing the variation in 200 μ M TCDCA-treated U251 cells compared with that in control-treated cells. **E** The mRNA expression of *HMGCS1*, *ASNS*, *GADD45A*, *HMGCR*, *LDL*, *MVD*, *ID11*, *CHAC1*, *ATF3* was detected in U251 cells after treated with 200 μ M TCDCA for 24 h by RT-qPCR (n = 3/group, t-test). **F** The expression of *HMGCS1* in U251 cells was detected after treated with 200 μ M TCDCA for 24 h by western blot. **G** The expression of *HMGCR* in U251 cells was detected after treated with 200 μ M TCDCA for 24 h by western blot. **H** Quantification analysis of the relative *HMGCS1* level as shown in **(G)** (normalized to control, n = 4/group, Mann–Whitney test). **I** Quantification analysis of the relative *HMGCR* level (normalize to control, n = 6/group, Mann–Whitney test) as shown in **(G)**. Data were mean + SEM. **P* < 0.05, ***P* < 0.01

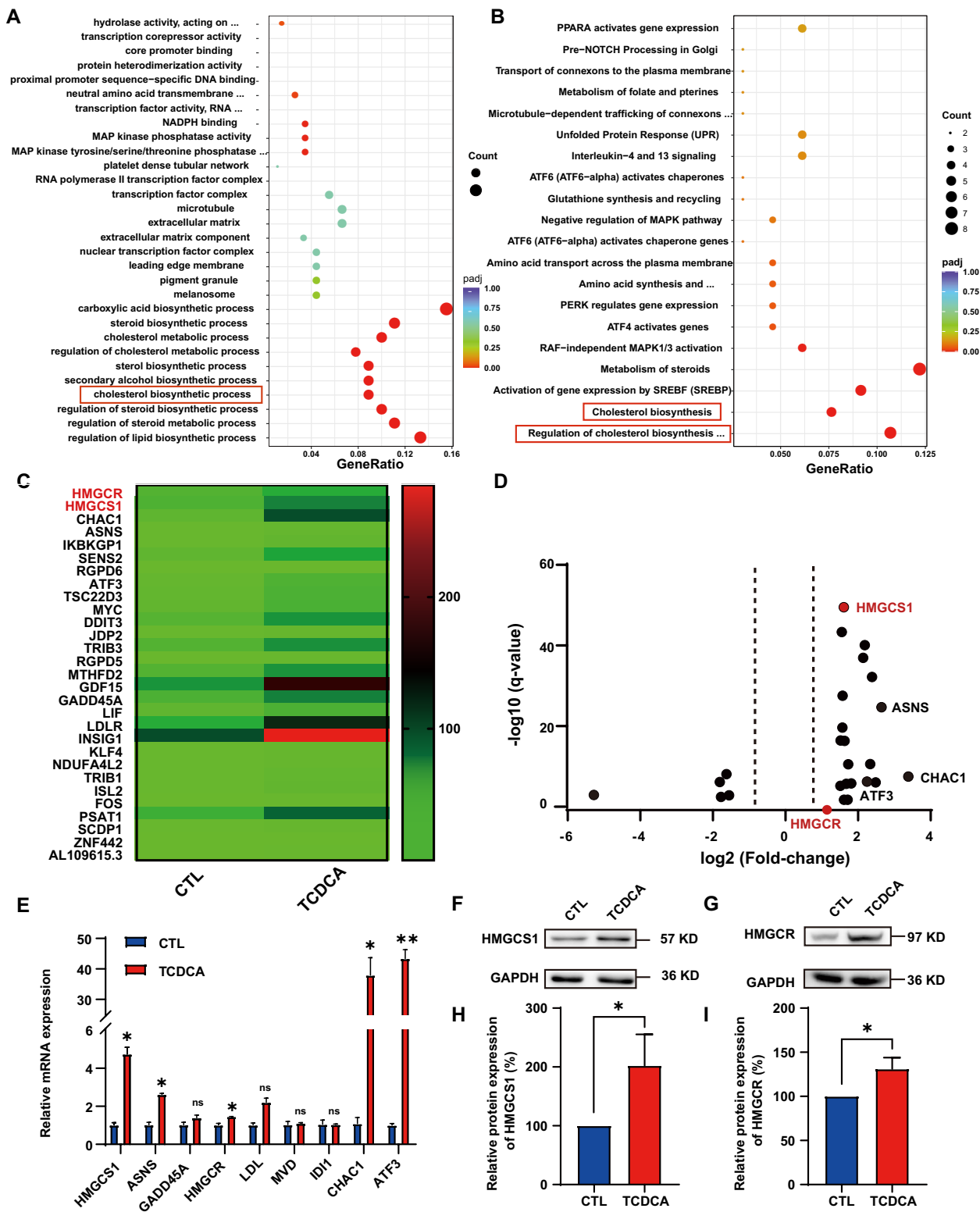


Fig. 3 (See legend on previous page.)

These results suggested that TCDCA induced cell cycle arrest at the G2/M phase of GBM cells.

TCDCA upregulated the signaling pathways of lipid biosynthetic process

To determine the exact mechanism of TCDCA in suppressing GBM cell proliferation and migration, mRNA sequencing was performed on U251 cells from the control as well as the TCDCA treated groups. Interestingly, when compared with the control group, TCDCA treatment altered expression of genes involved in several key biological processes including the cholesterol metabolism pathway, which was notably upregulated (GSE236200, Fig. 3A, B). To further confirm the differentially expressed genes in GBM cells treated with TCDCA, we analyzed the sequencing results and found that the expressions of HMGCS1, HMGCR, LDL and ASNS were significantly increased in TCDCA-treated U251 cells, all of which are related to cholesterol metabolism [51, 52] (Fig. 3C, D). Quantitative real-time PCR and western blot analysis were performed to validate the sequencing results. As shown in Fig. 3E–I, both mRNA and protein levels of HMGCS1 and HMGCR were increased in U251 cells after TCDCA treatment. Taken together, these results suggested that TCDCA upregulated the signaling pathways of lipid biosynthetic processes such as HMGCS1 and HMGCR expression. Given the expression of them were upregulated after TCDCA treatment, we hypothesized that HMGCS1 and HMGCR might function as repressors in GBM development. To verify this hypothesis, we first analyzed the integrated data from Gliovis database (<http://gliovis.bioinfo.cnio.es/>), and found that *HMGCS1* and *HMGCR* expressed lower in GBM tissues than that in the normal ones and the gene expression of *HMGCS1* and *HMGCR* decreased with the increase of malignant degree of glioma (Supplementary Fig. 2A–D). Furthermore, we analyzed the relevant survival curves, and found that high levels of *HMGCS1* and *HMGCR* were associated with favorable prognosis (Supplementary Fig. 2E–H). These results further suggested

that TCDCA might inhibit the progression of GBM by upregulating the expression of HMGCS1 and HMGCR.

TCDCA performed anti-GBM effects through upregulation of HMGCS1/HMGCR signaling pathway

To further confirm whether the TCDCA performs anti-GBM cell effects through up-regulating HMGCS1 and HMGCR signaling, the competitive inhibitor of HMGCR Simvastatin (SIN) was used to down-regulate the expression of HMGCS1 [53]. Since SIN, to a certain extent, has an inhibitory effect on the tumor cells itself [54], to eliminate this interference, we first conducted CCK-8 assay to determine the administration concentration of SIN. As shown in Fig. 4A, CCK-8 assay showed that 0.5 μ M SIN did not inhibit the proliferation of U251 cells, so we selected this concentration for the subsequent experiments. Treatment of U251 cells with TCDCA and SIN together significantly reversed the inhibitory effect of TCDCA on cell proliferation. As expected, the wound healing rate and the number of cells passing through the chamber in the Transwell assay were significantly increased in U251 cells treated with SIN and TCDCA together, compared with TCDCA treatment alone (Fig. 4B–E). Taken together, these results suggested that TCDCA performed anti-GBM effects through upregulating the expression of HMGCS1 and HMGCR. Western blot analysis was performed to validate the wound healing assay results. We then tested epithelial-mesenchymal transition-related indicators, and the results showed that the expression of related proteins in GL261 cells was decreased after TCDCA (Fig. 4F–J).

TCDCA suppressed GBM cells by inducing ferroptosis

Although we have found the effective targets of TCDCA, the exact pathway through which TCDCA achieves its anti-GBM effect remains to be clarified. We reanalyzed the sequencing results and found that many differentially expressed genes associated with ferroptosis [55], such as CHAC1, ATF3 and DDIT3 (Fig. 3B) were upregulated significantly after TCDCA

(See figure on next page.)

Fig. 4 TCDCA suppressed GBM cells through HMGCS1/HMGCR pathway. **A** The cell viability of U251 cells treated with different concentrations of 200 μ M TCDCA and SIN detected by CCK-8 assays ($n = 4$ /group, two-way ANOVA, Sidak's test was performed for the multiple comparison). **B** Representative images of U251 cells treated with 200 μ M TCDCA and 0.5 μ M SIN for 24 h in Transwell migration assay. Scale bar, 100 μ m. **C** Quantitative analysis of the numbers of migrated U251 cells ($n = 15$ /group, two-way ANOVA, Sidak's test was performed for the multiple comparison) and cells counted in representative high-power fields per Transwell plate. **D** Representative images of U251 cells treated with 200 μ M TCDCA and 0.5 μ M SIN in wound healing assays. Phase-contrast images were acquired at 0 h, 24 h after scratching and representative images of three independent experiments were shown. Scale bars, 200 μ m. **E** Quantitative analysis of the numbers of migrated U251 cells ($n = 15$ /group, two-way ANOVA, Sidak's test was performed for the multiple comparison) and cells counted in representative high-power fields per Transwell plate. **F** The expression of FAK, p-FAK, Vimentin and N-cadherin in GL261 cells was detected after treated with 200 μ M TCDCA for 24 h by western blot. **G–J** Quantification analysis of the relative FAK (**G**), p-FAK (**H**), Vimentin (**I**), N-cadherin (**J**) level as shown in (**F**) (normalized to control, $n = 3$ /group, t -test). Data were mean + SEM. * $P < 0.05$, ** $P < 0.01$

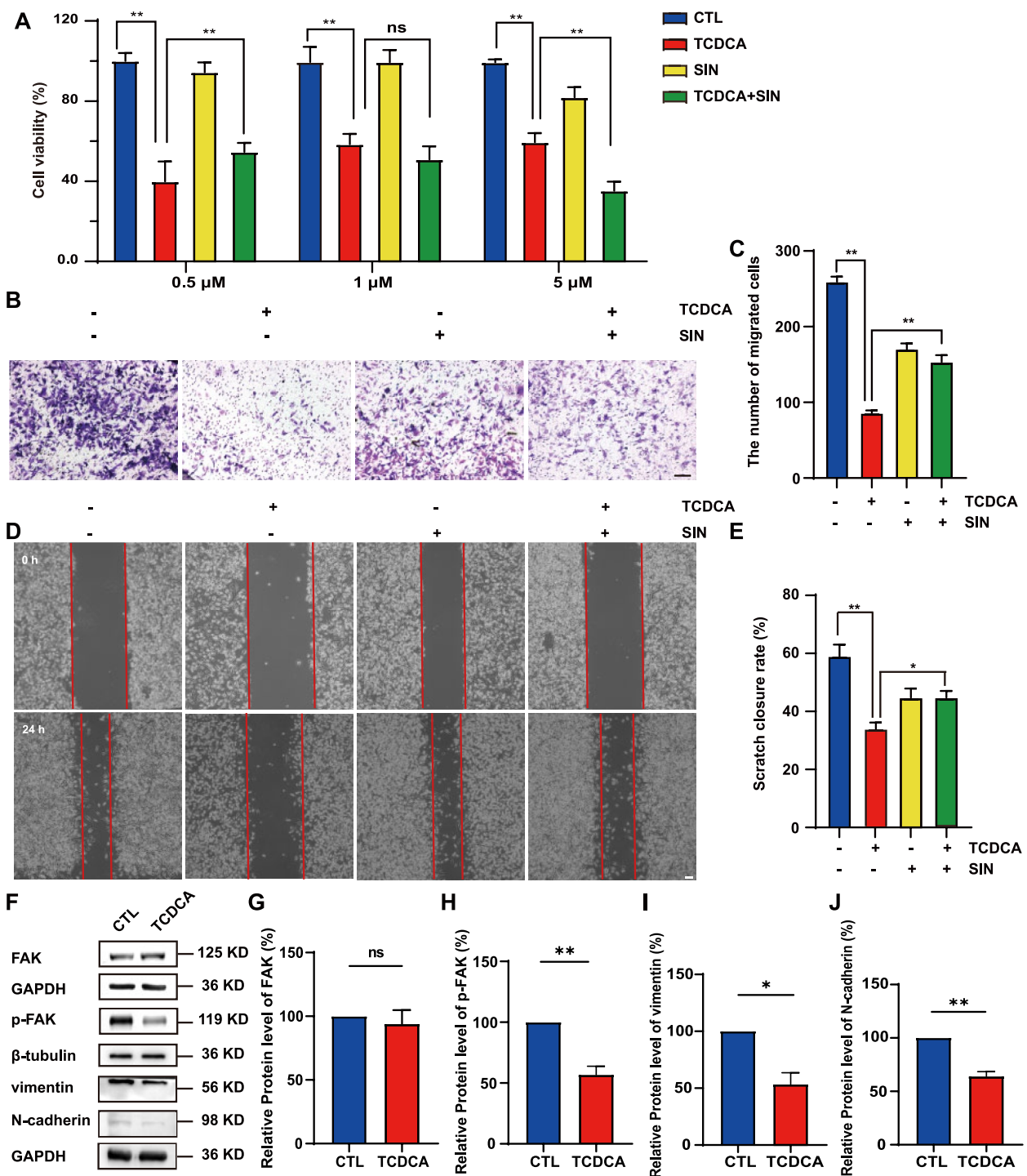


Fig. 4 (See legend on previous page.)

treatment. It is reasonable to speculate that TCDCA may inhibit the proliferation and migration of GBM cells by inducing ferroptosis. To test our hypothesis, we first examined protein levels of GPX4, a typical marker of ferroptosis that ferroptosis will be induced when it

is inhibited [56]. As expected, we found that TCDCA treatment resulted in downregulation of GPX4 (Fig. 5A, B). Ferroptosis is characterized by intracellular accumulation of lipid reactive oxygen species (ROS) in an iron-dependent manner [57, 58]. To clarify the impact

of TCDCA on ROS, we then detected the production of ROS after TCDCA treatment. Consistently, the results showed that treating U251 cells with TCDCA indeed remarkably induced the production of ROS (Fig. 5C, D). We further confirmed the role of TCDCA in inducing ferroptosis by adding ferrostatin-1 (FER-1, a classic ferroptosis inhibitor) in GBM cells. Firstly, U251 cells were treated with different concentrations of FER-1 by CCK-8 assay, and the cell viability curve analysis showed that 1.25 μ M of FER-1 could exert the greatest inhibitory effect on ferroptosis (Fig. 5E). Treatment of U251 cells with TCDCA and FER-1 together significantly reversed the inhibitory effect of TCDCA on cell proliferation. Furthermore, migration-related assays showed that the treatment with ferroptosis inhibitor could partially rescue the TCDCA's inhibitory effect on the migration of U251 cells (Fig. 5F–I). These results suggested that TCDCA induced ferroptosis in GBM cells by affecting GPX4 levels and ROS accumulation.

TCDCA induced ferroptosis in GBM cells through HMGCS1-HMGCR-GPX4 pathway

However, it is still unclear whether drugs can inhibit GBM progression by regulating the expression of HMGCS1 and HMGCR to induce ferroptosis directly. To address this question, we then examined the changes of ferroptosis-related markers after inhibiting HMGCS1 and HMGCR. First, western blot analysis showed that co-treatment of SIN and TCDCA partially abolished the ferroptosis in U251 cells induced by TCDCA treatment alone (Fig. 6A–D). Next, we detected the amount of intracellular ROS production after inhibiting the expression of HMGCS1 and HMGCR. As expected, the results showed that treatment with SIN together could effectively reduce the accumulation of ROS caused by TCDCA (Fig. 6E, F). GSH is the most important antioxidant to repair the damage in cell membrane caused by lipid hydroperoxides and clean the ROS [59]. The result of GSH detection was consistent with expectation, and the inhibitory effect of TCDCA on GSH could be

reversed by SIN (Fig. 6G). Taken together, these results strongly suggested that TCDCA induced ferroptosis in GBM cells through HMGCS1-HMGCR-GPX4 pathway.

TCDCA inhibited the growth of GBM in vivo

Given in vitro experiments showing TCDCA's significant anti-GBM activities, we next examined whether TCDCA also had anti-tumor effects in vivo. We examined the effect of TCDCA in an orthotopic transplantation model of GBM cells in C57BL/6 mice. Firstly, we injected GL261 cells (a mice GBM cell line) with the luciferase reporter gene into the striatum of C57BL/6 mice by using a brain stereotaxic apparatus. Seven days after modeling, we randomly divided the mice into two experimental groups: the control group (0.9% saline) and the TCDCA group (30 mg/kg), and both groups received an intraperitoneal injection for 14 days (Fig. 7A). By recording and analyzing the weight data of mice during the administration, we found that there was no significant difference in the weight changes of mice (Fig. 7B). Tumor formation was observed by small animal 3D bioluminescence imaging system, and it was found that TCDCA treatment significantly inhibited GBM volume (Fig. 7C, D). Hematoxylin–eosin (HE) and Ki67 staining were performed on frozen slices of mouse brain tissue, and the results further showed anti-GBM of TCDCA in vivo (Fig. 7E–H) and TCDCA is not toxic to the heart, liver, spleen, lung and kidney of mice (Supplementary Fig. 3). In addition, the expression of HMGCS1 and HMGCR was upregulation while GPX4 was downregulation in orthotopic model mice (Fig. 7I–L), demonstrating that TCDCA also inhibited the growth of GBM cells dependent on HMGCS1/HMGCR/GPX4 signaling in vivo. Taken together, these results suggested that TCDCA inhibited GBM growth in vivo effectively.

Discussion

Our studies have revealed the inhibitory effects of TCDCA on GBM cell proliferation and migration. We have shown that TCDCA achieves these effects through

(See figure on next page.)

Fig. 5 TCDCA suppressed GBM cells through inducing ferroptosis. **A** Western blot detected the expression of GPX4 in U251 cells treated with 200 μ M TCDCA. **B** Quantification of the relative level of GPX4 as shown in **(A)** ($n=4$ per group, t -test). **C** Representative results of ROS analysis in U251 cells after 200 μ M TCDCA treatment. **D** Quantitative analysis of ROS in U251 cells as shown in **(C)** ($n=3$ /group, t -test). **E** The cell viability of U251 cells treated with different concentrations of FER-1 and 200 μ M TCDCA detected by CCK-8 assays ($n=4$ /group, two-way ANOVA, Sidak's test was performed for the multiple comparison). **F** Representative images of U251 cells treated with 200 μ M TCDCA and 1.25 μ M FER-1 in wound healing assays. Phase-contrast images were acquired at 0 h, 24 h after scratching and representative images of three independent experiments were shown. Scale bars, 200 μ m. **G** Quantitative analysis of the numbers of migrated U251 cells ($n=15$ /group, two-way ANOVA, Sidak's test was performed for the multiple comparison) and cells counted in representative high-power fields per Transwell plate. **H** Representative images of U251 cells treated with 200 μ M TCDCA and 1.25 μ M FER-1 for 24 h in Transwell migration assay. Scale bar, 100 μ m. **I** Quantitative analysis of the numbers of migrated U251 cells and cells counted in representative high-power fields per Transwell plate ($n=15$ /group, two-way ANOVA, Sidak's test was performed for the multiple comparison). Data were mean + SEM. * $P<0.05$, ** $P<0.01$

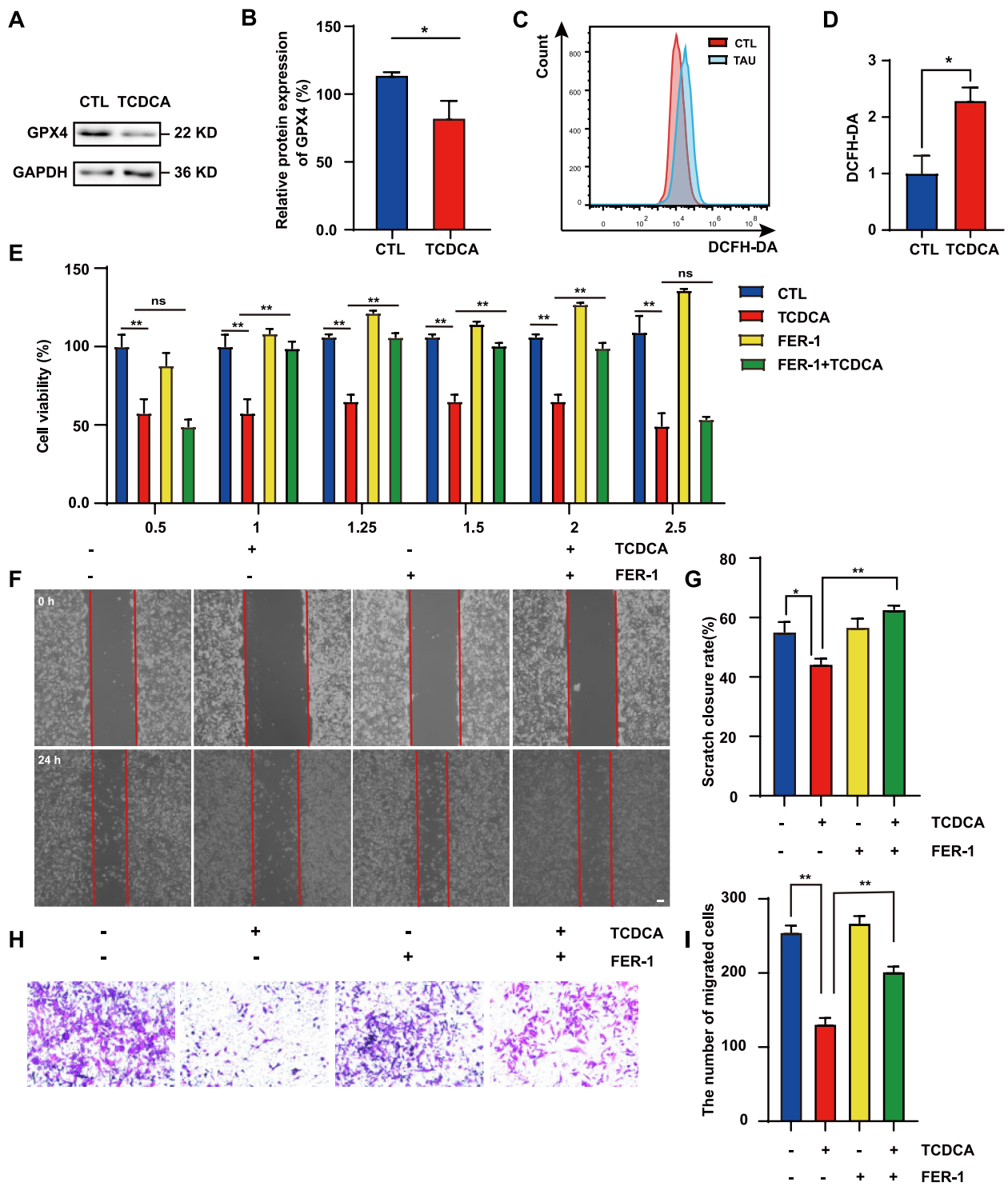


Fig. 5 (See legend on previous page.)

the modulation of the HMGCS1-HMGCR-GPX4 signaling pathway in vivo and in vitro (Fig. 8). These results provide the potential of TCDCA as an efficacious therapeutic agent for alleviating GBM.

Extensive researches, over the past decades, has elucidated metabolic reprogramming in glioma and the therapeutic relevance of metabolic dependence [60], including the identification of potential metabolic biomarkers and

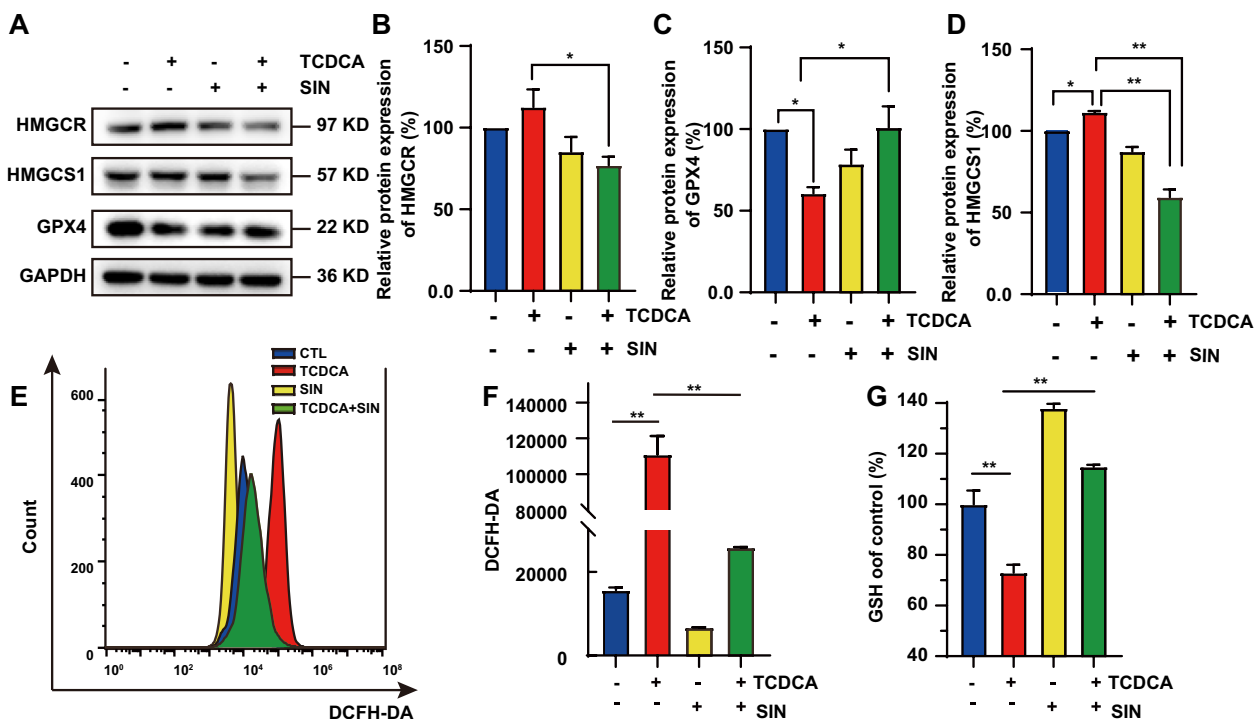


Fig. 6 TCDCA induced ferroptosis of GBM cells through HMGCS1-HMGCR-GPX4 pathway. **A** Western blot detected the expression of HMGCS1, HMGCR and GPX4 in U251 cells treated with 200 μ M TCDCA and SIN. **B–D** Quantification of the relative level of HMGCR (**B**), HMGCR (**B**) (normalized to control, n = 5/per group, two-way ANOVA, Sidak’s test) and GPX4 (**C**) (normalized to control, n = 6/per group, two-way ANOVA, Sidak’s test) and HMGCS1 (**D**) (n = 6/per group, two-way ANOVA, Sidak’s test) as shown in (**A**). **E** Representative results of ROS analysis in U251 cells after 200 μ M TCDCA and 0.5 μ M SIN treatment. **F** Quantitative analysis of ROS in U251 cells (n = 3/group, two-way ANOVA, Sidak’s test) as shown in (**E**). **G** Quantification of the relative level of GSH (n = 3/group, two-way ANOVA, Sidak’s test). Data were mean + SEM. **P* < 0.05, ***P* < 0.01

therapeutic targets. Lipids, constituting vital components of brain structure and function [61], possess the second-highest content in the brain following adipose tissue [62]. Notably, almost all brain cholesterol is synthesized by astrocytes, as systemic cholesterol in lipoproteins faces significant BBB permeability challenges [63]. Cholesterol levels are regulated by various factors, including metabolites and bile acids [64]. Ursodeoxycholic acid (UDCA), a hydrophilic bile acid, has been studied for its application in cancer [65]. Ursodeoxycholic acid is the trans-isomer of chenodeoxycholic acid. TCDCA, the taurine-conjugated form of chenodeoxycholic acid [66], emerges as an integral derivative with reduced toxicity and enhanced solubility. Studies have shown through in vitro and in vivo experiments that TCDCA can inhibit the progression of gastric cancer [42]. While prior investigations have focused primarily on TCDCA’s pro-apoptotic, anti-inflammatory and immunomodulatory effects, its pharmacological effect on GBM remains largely unexplored. Similar to previous studies, in this study, we found that TCDCA significantly inhibited the progression of GBM in vitro and in vivo.

As a non-apoptotic form of cell death, ferroptosis is a result of an imbalance in cellular metabolism and redox homeostasis [67]. Meanwhile, accumulating evidence suggests that there is a potential physiological role of ferroptosis in anti-tumor therapy [68]. Both GSH depletion and GPX4 inactivation induce ferroptosis. However, it remains unknown whether TCDCA has anti-GBM effects via inducing ferroptosis. Cholesterol metabolism assumes a pivotal role in orchestration of ferroptosis [69], with evidence showcasing the involvement of that 7-dehydrocholesterol reductase, an enzyme governing cholesterol biosynthesis, in ferroptosis induction [70]. Statin treatment has been correlated with elevated levels of cellular lipid peroxidation [71]. Studies have shown that GBM cells are resistant to statin targeting HMGCR, and promoting cholesterol synthesis can inhibit the development of glioma [36]. In this study, we explored whether TCDCA induced significant alterations in HMGCS1, HMGCR, directly impacting ferroptosis-related targets and effectively impeded GBM progression. Although this study verified the inhibitory effect of TCDCA on GBM in vivo and in vitro, the mechanism of TCDCA’s action was only studied in vitro, and there

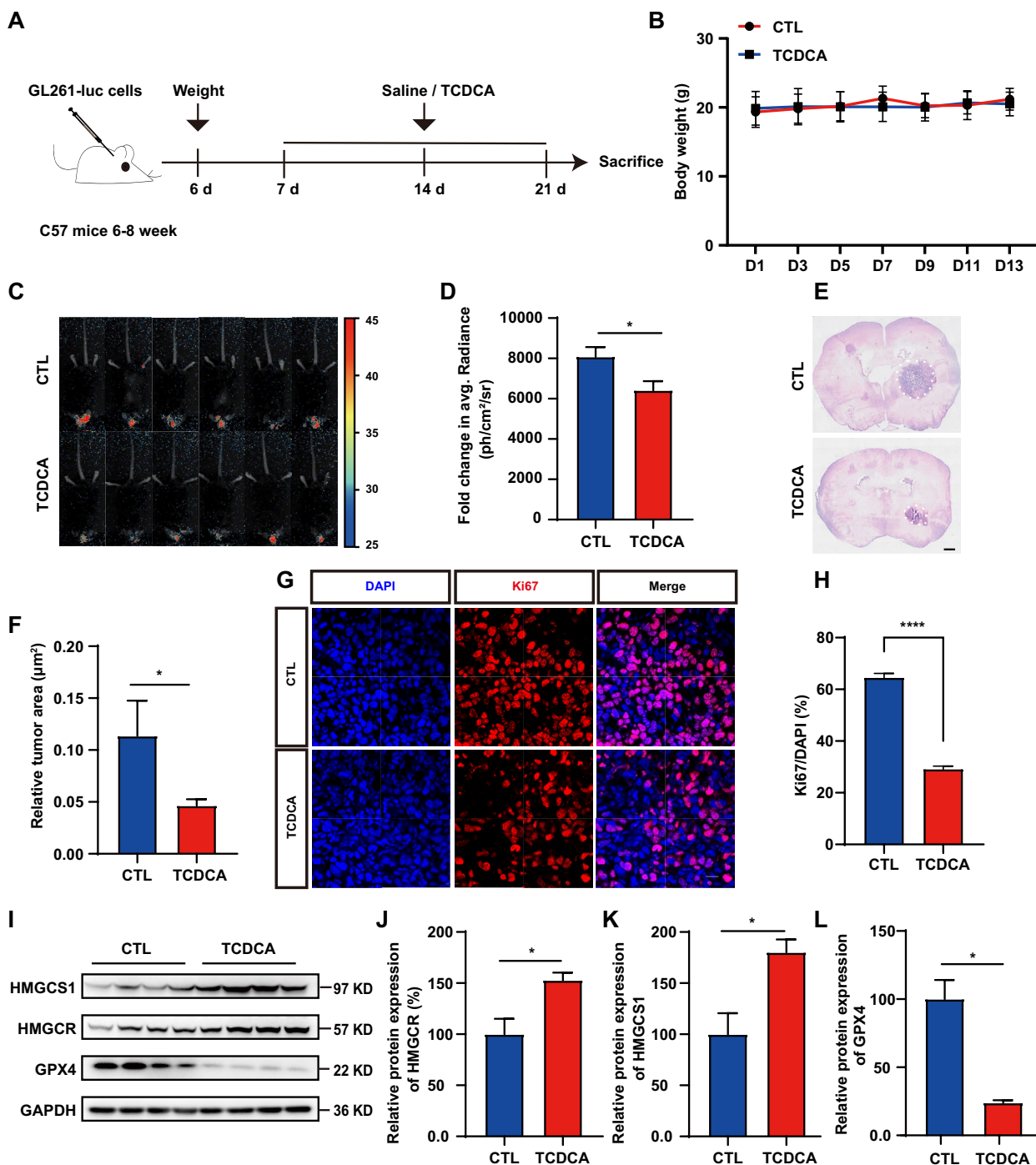


Fig. 7 TCDCA inhibited the growth of GBM in vivo. **A** Experimental Scheme for orthotopic GBM mice model. **B** The body weight of the tumor-bearing mice was monitored every day (n=6 mice, per group). **C** Bioluminescent imaging of disseminated GL261-Luc orthotopic xenograft mice at different time points posttreatment with TCDCA and the control. **D** Fold change in average radiance mouse at experimental endpoint was analyzed for each treatment group (n=6/group, t-test). **E** Representative images of HE staining of whole-brain sections from TCDCA and control-treated group. Scale bar, 1 mm. **F** Quantification analysis of the area of GBM in (E) (normalized to control, n=4/group, t-test). **G** Representative images of Ki67 staining of whole-brain sections from TCDCA and control-treated group. Scale bar, 20 μm. **H** Quantification analysis of the area of GBM in (G) (normalized to control, n=9/group, t-test). **I** Western blot detected the expression of HMGCS1, HMGCR and GPX4 in orthotopic tumor tissue. **J–L** Quantification of the relative level of HMGCS1 (J), HMGCR (K) and GPX4 (L) as shown in (G) (normalized to control, n=4/per group, t-test). Data were mean + SEM. *****P* < 0.0001, **P* < 0.05

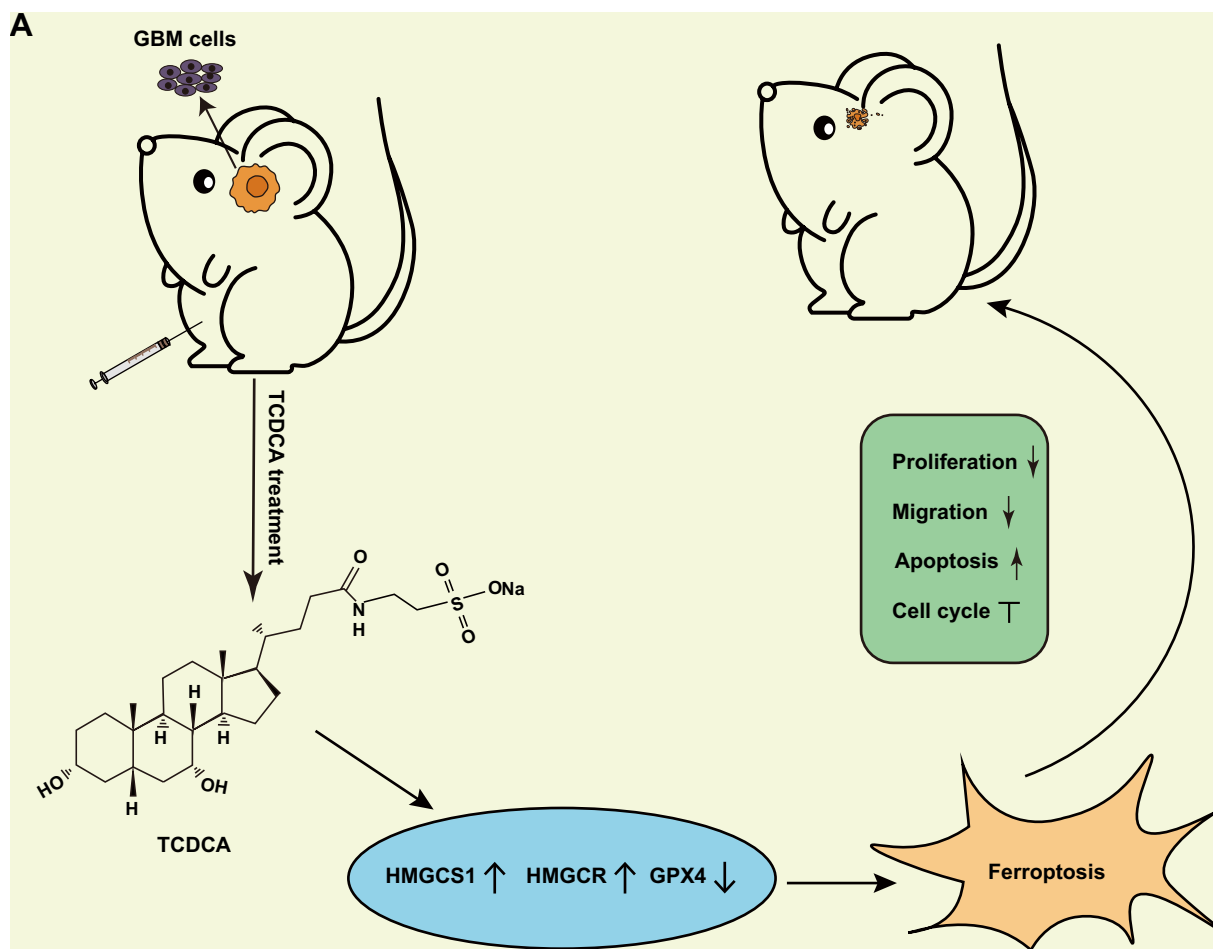


Fig. 8 A working model of TCDCA in GBM cells. TCDCA suppresses the progression of GBM via HMGC1/HMGC1R/GPX4 signaling axis, which may result in inhibiting the tumorigenesis, including inhibition of cell proliferation, migration, and induction of the apoptosis and cell cycle arrest both in vitro and in vivo

is a lack of rescue experiments in vivo to confirm that TCDCA played a role by regulating HMGC1-HMGC1R-GPX4 pathway.

While implanting GL261 cells in the mouse brain is a widely used method for constructing GBM models in neuro-oncology research, it has several limitations that need to be considered. The GBM model in our study was generated through cell line implantation, which did not replicate the natural progression of tumors from early gene mutations to malignant transformation. This method may result in significant differences in the tumor microenvironment compared to human GBM, which typically has a highly immunosuppressive TME [72]. Human GBM is characterized by high intratumoral heterogeneity, including the coexistence of different subclones. In contrast, the GL261 cell line, derived from a monoclonal source, lacks this heterogeneity, potentially leading to underestimation of the risk of drug resistance during drug screening. Long-term

in vitro subculturing of GL261 cells may also result in the loss of the original tumor’s heterogeneity. Additionally, variability in the implantation site may impact the reproducibility of experimental results. Despite these limitations, the GL261 in situ glioma model remains valuable for its cost-effectiveness, ease of operation, and suitability for high-throughput screening. It continues to play an important role in immune research and drug screening.

Although this study confirmed the key role of the HMGC1/HMGC1R/GPX4 pathway in GBM, several limitations remain. It is not clear whether TCDCA regulates these targets directly or indirectly, for example, through nuclear receptors such as FXR or PXR, or via the membrane receptor TGR5. Additionally, the involvement of other lipid metabolism or oxidative stress-related pathways (such as SREBP or NRF2) cannot be ruled out. While our study has preliminarily demonstrated the feasibility of using TCDCA to inhibit GBM via the

HMGCS1/HMGCR/GPX4 pathway, further research is needed to elucidate the underlying mechanisms, validate the clinical relevance of the model, and develop effective translational strategies. In the future, TCDCA holds potential for clinical application through multi-dimensional mechanistic analysis, precise modeling, and the development of intelligent drug delivery technologies. These efforts will be crucial for advancing our understanding and treatment of GBM.

In a study, serum levels of TCDCA were significantly lower in patients with hepatitis B virus (HBV)-related hepatocellular carcinoma (HCC) and closely correlated with tumor progression [73]. Additionally, research has shown that TCDCA significantly inhibits the viability and invasive capacity of gastric cancer cells while inducing apoptosis. This anticancer effect is mediated through the downregulation of key genes such as REG4, EGFR, and AKT1 [74].

In summary, the present study has substantiated the profound anti-GBM effects exerted by TCDCA via HMGCS1-HMGCR-GPX4 pathway both in vitro and in vivo. Our study further confirms that targeted cholesterol metabolism may be a useful anti-GBM therapy and provides a potential anti-GBM drug. The action value of the traditional Chinese medicine extract is further developed, which not only has clinical treatment potential but also can bring certain social and economic benefits.

Supplementary Information

The online version contains supplementary material available at <https://doi.org/10.1186/s12935-025-03782-2>.

Supplementary Material 1: Figure S1. Toxicity detection of solvents and drugs. (A) The cell viability of GL261 cells treated with 0.2% DMSO. (B) The cell viability of HT22 cells treated with 200 μ m TCDCA. Data were mean \pm SEM. *ns* $P > 0.05$, *ns* $P > 0.05$.

Supplementary Material 2: Figure S2. The expression of HMGCS1 and HMGCR was associated with glioma grade and survival. (A-B) Analysis of HMGCS1 (left) and HMGCR (right) in GBMs versus normal brain from CGGA gene expression data. (C-D) Analyzing the expression of HMGCS1 (left) and HMGCR (right) in glioma tissues of different grades. (E-H) Represent the correlation between the levels of HMGCS1 (E-F) and HMGCR (G-H) with patient survival in primary and secondary gliomas.

Supplementary Material 3: Figure S3. HE staining of heart, liver, spleen, lung and kidney of mice after TCDCA treatment.

Author contributions

Xiumin Xue, Ziwan He and Furui Liu: Conceptualization, analysis, visualization, validation, and writing the manuscript; Qian Wang, Zhichao Chen, Lin Lin, Danni Chen, Yinfeng Yuan: Data curation, analysis, software, and visualization; Zhihui Huang, Yongjie Wang: Conceptualization, methodology design, project administration, supervision, funding acquisition, and writing review & editing.

Funding

This work was supported by the General scientific research project of Zhejiang Provincial Department of Education in 2022 (Y202250540).

Availability of data and materials

Data generated and analyzed in this study are included in the manuscript and supplementary files. Additional information is available from the corresponding author on reasonable request.

Declarations

Ethics approval and consent to participate

The Animal Care and Use Committee at Hangzhou Normal University granted consent to all animal research, and the approval number is HSD20220105.

Competing interests

The authors declare no competing interests.

Received: 24 October 2024 Accepted: 4 April 2025

Published online: 22 April 2025

References

- Tan AC, et al. Management of glioblastoma: state of the art and future directions. *CA Cancer J Clin*. 2020;70(4):299–312.
- Wirsching H-G, Galanis E, Weller M. Glioblastoma. In *Gliomas*. 2016. p. 381–397.
- DeCordova S, et al. Molecular heterogeneity and immunosuppressive microenvironment in glioblastoma. *Front Immunol*. 2020;11:1402.
- Sun S, et al. Atractylon inhibits the tumorigenesis of glioblastoma through SIRT3 signaling. *Am J Cancer Res*. 2022;12(5):2310–22.
- Martikainen M, Essand M. Virus-based immunotherapy of glioblastoma. *Cancers (Basel)*. 2019. <https://doi.org/10.3390/cancers11020186>.
- Aliferis C, Trafalis DT. Glioblastoma multiforme: pathogenesis and treatment. *Pharmacol Ther*. 2015;152:63–82.
- Xu J, et al. Irigenin inhibits glioblastoma progression through suppressing YAP/ β -catenin signaling. *Front Pharmacol*. 2022;13:1027577.
- Li J, et al. Nanoparticle drug delivery system for glioma and its efficacy improvement strategies: a comprehensive review. *Int J Nanomed*. 2020;15:2563–82.
- Dréan A, et al. Blood-brain barrier, cytotoxic chemotherapies and glioblastoma. *Expert Rev Neurother*. 2016;16(11):1285–300.
- Zhu J, et al. Combination of chemotherapy and gaseous signaling molecular therapy: novel β -elemene nitric oxide donor derivatives against leukemia. *Drug Dev Res*. 2023;84(4):718–35.
- Zou Y, et al. The triangular relationship between traditional Chinese medicines, intestinal flora, and colorectal cancer. *Med Res Rev*. 2024;44(2):539–67.
- Zhu J, et al. Discovery and bioassay of disubstituted β -elemene-NO donor conjugates: synergistic enhancement in the treatment of leukemia. *Chin J Nat Med*. 2023;21(12):916–26.
- Wei M-M, et al. A combination index and glycoproteomics-based approach revealed synergistic anticancer effects of curcuminoids of turmeric against prostate cancer PC3 cells. *J Ethnopharmacol*. 2021;267:113467.
- Lou J-S, et al. Ginkgetin derived from Ginkgo biloba leaves enhances the therapeutic effect of cisplatin via ferroptosis-mediated disruption of the Nrf2/HO-1 axis in EGFR wild-type non-small-cell lung cancer. *Phytomedicine*. 2021;80:153370.
- Kong N, et al. Baicalin induces ferroptosis in bladder cancer cells by downregulating FTH1. *Acta Pharm Sin B*. 2021;11(12):4045–54.
- Sun Y, et al. Jatrorrhizine inhibits mammary carcinoma cells by targeting TNIK mediated Wnt/ β -catenin signalling and epithelial-mesenchymal transition (EMT). *Phytomedicine*. 2019. <https://doi.org/10.1016/j.phymed.2019.153015>.
- Hui Z, et al. Discovery of plant-derived anti-tumor natural products: potential leads for anti-tumor drug discovery. *Bioorg Chem*. 2024;142:106957.

18. Bai R, et al. Second generation β -elemene nitric oxide derivatives with reasonable linkers: potential hybrids against malignant brain glioma. *J Enzyme Inhib Med Chem*. 2022;37(1):379–85.
19. Zhao L-P, et al. Hyperprogression, a challenge of PD-1/PD-L1 inhibitors treatments: potential mechanisms and coping strategies. *Biomed Pharmacother*. 2022;150: 112949.
20. Duan J-L, et al. Design, synthesis, and structure-activity relationship of novel pyridazinone-based PARP7/HDACs dual inhibitors for elucidating the relationship between antitumor immunity and HDACs inhibition. *J Med Chem*. 2024;67(6):4950–76.
21. Chen L, et al. The roles and mechanism of m6A RNA methylation regulators in cancer immunity. *Biomed Pharmacother*. 2023;163: 114839.
22. Qiu Z, et al. The role and therapeutic potential of macropinocytosis in cancer. *Front Pharmacol*. 2022. <https://doi.org/10.3389/fphar.2022.919819>.
23. Hu J, et al. Emerging advances in engineered macrophages for tumor immunotherapy. *Cytotherapy*. 2023;25(3):235–44.
24. Liu S, et al. The mechanism of m6A methyltransferase METTL3-mediated autophagy in reversing gefitinib resistance in NSCLC cells by β -elemene. *Cell Death Dis*. 2020;11(11):969.
25. Zhao J, et al. Tumor cell membrane-coated continuous electrochemical sensor for GLUT1 inhibitor screening. *J Pharm Anal*. 2023;13(6):673–82.
26. Torres MP, et al. Graviola: a novel promising natural-derived drug that inhibits tumorigenicity and metastasis of pancreatic cancer cells in vitro and in vivo through altering cell metabolism. *Cancer Lett*. 2012;323(1):29–40.
27. Berrak Ö, et al. The inhibition of PI3K and NF κ B promoted curcumin-induced cell cycle arrest at G2/M via altering polyamine metabolism in Bcl-2 overexpressing MCF-7 breast cancer cells. *Biomed Pharmacother*. 2016;77:150–60.
28. Liang X-J, et al. SIRT1 contributes in part to cisplatin resistance in cancer cells by altering mitochondrial metabolism. *Mol Cancer Res*. 2008;6(9):1499–506.
29. Song G-Q, et al. Elemene induces cell apoptosis via inhibiting glutathione synthesis in lung adenocarcinoma. *J Ethnopharmacol*. 2023;311: 116409.
30. Murai T. Cholesterol lowering: role in cancer prevention and treatment. *Biol Chem*. 2015;396(11):1–11.
31. Pirmoradi L, et al. Targeting cholesterol metabolism in glioblastoma: a new therapeutic approach in cancer therapy. *J Investig Med*. 2019;67(4):715–9.
32. Turri M, et al. Emerging role of HDL in brain cholesterol metabolism and neurodegenerative disorders. *Biochim Biophys Acta BBA Mol Cell Biol Lipids*. 2022;1867(5): 159123.
33. Hwang S, et al. Contribution of accelerated degradation to feedback regulation of 3-hydroxy-3-methylglutaryl coenzyme a reductase and cholesterol metabolism in the liver. *J Biol Chem*. 2016;291(26):13479–94.
34. Ho WY, Hartmann H, Ling S-C. Central nervous system cholesterol metabolism in health and disease. *IUBMB Life*. 2022;74(8):826–41.
35. Ding X, et al. The role of cholesterol metabolism in cancer. *Am J Cancer Res*. 2019;9(2):219–27.
36. Villa GR, et al. An LXR-cholesterol axis creates a metabolic co-dependency for brain cancers. *Cancer Cell*. 2016;30(5):683–93.
37. Russell DW. The enzymes, regulation, and genetics of bile acid synthesis. *Annu Rev Biochem*. 2003;72(1):137–74.
38. Wang X, et al. Taurochenodeoxycholic acid induces NR8383 cells apoptosis via PKC/JNK-dependent pathway. *Eur J Pharmacol*. 2016;786:109–15.
39. McGlone ER, Bloom SR. Bile acids and the metabolic syndrome. *Ann Clin Biochem*. 2019;56(3):326–37.
40. Li L, et al. Taurochenodeoxycholic acid inhibited AP-1 activation via stimulating glucocorticoid receptor. *Molecules*. 2019. <https://doi.org/10.3390/molecules24244513>.
41. He X, et al. Effect of taurochenodeoxycholic acid on immune function in mice. *Zhong yao cai Zhongyaoacai J Chin Med Mater*. 2005;28(12):1089–92.
42. Zhang D, et al. Taurochenodeoxycholic acid inhibits the proliferation and invasion of gastric cancer and induces its apoptosis. *J Food Biochem*. 2022;46(3): e13866.
43. Zhang M, et al. Rapid separation of bile acid isomers via ion mobility mass spectrometry by complexing with spiramycin. *Anal Bioanal Chem*. 2024;416(28):6563–73.
44. Nuo X, Bai Y, Han X, Yuan J, Wang L, He Y, Yang L, Hui W, Shi H, Xiaojun W. Taurochenodeoxycholic acid reduces astrocytic neuroinflammation and alleviates experimental autoimmune encephalomyelitis in mice. *Immunobiology*. 2023;228(3): 152388.
45. Jacob F, et al. A patient-derived glioblastoma organoid model and biobank recapitulates inter- and intra-tumoral heterogeneity. *Cell*. 2020;180(1):188–204.e22.
46. Venkataramani V, et al. Glioblastoma hijacks neuronal mechanisms for brain invasion. *Cell*. 2022;185(16):2899–2917.e31.
47. Li J, et al. Active targeting of orthotopic glioma using biomimetic liposomes co-loaded elemene and cabazitaxel modified by transferin. *Journal of Nanobiotechnology*. 2021;19(1):289.
48. Ogura Y, Sasakura Y. Cell-cycle compensation coupled with developmental patterning. *Cell Cycle*. 2016;15(20):2685–6.
49. Strzyp P. Signalling to cell cycle arrest. *Nat Rev Mol Cell Biol*. 2016;17(9):536–536.
50. Petrachkova T, et al. Lack of Cyclin B1 in zebrafish causes lengthening of G2 and M phases. *Dev Biol*. 2019;451(2):167–79.
51. Wang B, et al. Ferroptosis-related biomarkers for Alzheimer's disease: identification by bioinformatic analysis in hippocampus. *Front Cell Neurosci*. 2022. <https://doi.org/10.3389/fncel.2022.1023947>.
52. Battaglia AM, et al. Ferroptosis and cancer: mitochondria meet the "iron maiden" cell death. *Cells*. 2020. <https://doi.org/10.3390/cells9061505>.
53. Shen Y, et al. Activation of mitochondrial unfolded protein response in SHSY5Y expressing APP cells and APP/PS1 mice. *Front Cell Neurosci*. 2020. <https://doi.org/10.3389/fncel.2019.00568>.
54. Relja B, et al. Simvastatin inhibits cell growth and induces apoptosis and G0/G1 cell cycle arrest in hepatic cancer cells. *Int J Mol Med*. 2010;26(5):735–41.
55. Zhang H, et al. 5-Hydroxymethylfurfural alleviates inflammatory lung injury by inhibiting endoplasmic reticulum stress and NLRP3 inflammation activation. *Front Cell Dev Biol*. 2021. <https://doi.org/10.3389/fcell.2021.782427>.
56. Seibt TM, Proneth B, Conrad M. Role of GPX4 in ferroptosis and its pharmacological implication. *Free Radical Biol Med*. 2019;133:144–52.
57. Sui X, et al. RSL3 drives ferroptosis through GPX4 inactivation and ROS production in colorectal cancer. *Front Pharmacol*. 2018. <https://doi.org/10.3389/fphar.2018.01371>.
58. Niu B, et al. Application of glutathione depletion in cancer therapy: enhanced ROS-based therapy, ferroptosis, and chemotherapy. *Biomaterials*. 2021;277: 121110.
59. Ursini F, Maiorino M. Lipid peroxidation and ferroptosis: the role of GSH and GPx4. *Free Radic Biol Med*. 2020;152:175–85.
60. Masui K, et al. Metabolic reprogramming in the pathogenesis of glioma: update. *Neuropathology*. 2019;39(1):3–13.
61. Yoon JH, et al. Brain lipidomics: from functional landscape to clinical significance. *Sci Adv*. 2022;8(37):9317.
62. Bruce KD, Zsombok A, Eckel RH. Lipid processing in the brain: a key regulator of systemic metabolism. *Front Endocrinol*. 2017. <https://doi.org/10.3389/fendo.2017.00060>.
63. Bi J, et al. Altered cellular metabolism in gliomas—an emerging landscape of actionable co-dependency targets. *Nat Rev Cancer*. 2020;20(1):57–70.
64. Nguyen JT, Shaw RPH, Anakk S. Bile acids—a peek into their history and signaling. *Endocrinology*. 2022;163(11):bqac155.
65. Yao Z, et al. Ursodeoxycholic acid inhibits glioblastoma progression via endoplasmic reticulum stress related apoptosis and synergizes with the proteasome inhibitor bortezomib. *ACS Chem Neurosci*. 2020;11(9):1337–46.
66. Kusaczuk M. Tauroursodeoxycholate—bile acid with chaperoning activity: molecular and cellular effects and therapeutic perspectives. *Cells*. 2019. <https://doi.org/10.3390/cells8121471>.
67. Sun Y, et al. The emerging role of ferroptosis in inflammation. *Biomed Pharmacother*. 2020;127: 110108.
68. Wang Y, et al. The function and mechanism of ferroptosis in cancer. *Apoptosis*. 2020;25(11):786–98.
69. Xu H, et al. Cholesterol metabolism: new functions and therapeutic approaches in cancer. *Biochim Biophys Acta BBA Rev Cancer*. 2020;1874(1): 188394.
70. Liang D, Minikes AM, Jiang X. Ferroptosis at the intersection of lipid metabolism and cellular signaling. *Mol Cell*. 2022;82(12):2215–27.

71. Viswanathan VS, et al. Dependency of a therapy-resistant state of cancer cells on a lipid peroxidase pathway. *Nature*. 2017;547(7664):453–7.
72. DeCordova S, et al. Molecular heterogeneity and immunosuppressive microenvironment in glioblastoma. *Front Immunol*. 2020. <https://doi.org/10.3389/fimmu.2020.01402>.
73. Dai S, et al. Alteration of serum bile acid profiles of HBV-related hepatocellular carcinoma identified by LC–MS/MS. *J Cancer Res Clin Oncol*. 2024. <https://doi.org/10.1007/s00432-024-05686-6>.
74. Zhang D, et al. Taurochenodeoxycholic acid inhibits the proliferation and invasion of gastric cancer and induces its apoptosis. *J Food Biochem*. 2021. <https://doi.org/10.1111/jfbc.13866>.

Publisher's Note

Springer Nature remains neutral with regard to jurisdictional claims in published maps and institutional affiliations.